School of Natural Sciences and Mathematics

Effects of Electric Field Methods on Modeling the Midlatitude Ionospheric Electrodynamics and Inner Magnetosphere Dynamics

UT Dallas Author(s):

Roderick A. Heelis

Citation:

Yu, Yiqun, Vania K. Jordanova, Aaron J. Ridley, Gabor Toth, et al. 2017. "Effects of electric field methods on modeling the midlatitude ionospheric electrodynamics and inner magnetosphere dynamics." Journal of Geophysical Research--Space Physics 122(5), doi:10.1002/2016JA023850

AGU PUBLICATIONS

JGR

Journal of Geophysical Research: Space Physics

RESEARCH ARTICLE

10.1002/2016JA023850

Key Points:
- Self-consistent treatment of electric field now included in the kinetic ring current model RAM-SCB-E, advanced from previous empirical model
- Self-consistent electric field reproduced observed dynamic spatial distribution of local electric field enhancement in the dusk sector
- Self-consistent electric field method captured subauroral polarization streams (SAPS)

Correspondence to:
Y. Yu,
yiqunyu17@gmail.com

Citation:
Yu, Y., V. K. Jordanova, A. J. Ridley, G. Toth, and R. Heelis (2017), Effects of electric field methods on modeling the midlatitude ionospheric electrodynamics and inner magnetosphere dynamics, *J. Geophys. Res. Space Physics*, *122*, 5321–5338, doi:10.1002/2016JA023850.

Received 27 DEC 2016
Accepted 3 MAY 2017
Accepted article online 10 MAY 2017
Published online 22 MAY 2017

Effects of electric field methods on modeling the midlatitude ionospheric electrodynamics and inner magnetosphere dynamics

Yiqun Yu[1], Vania K. Jordanova[2], Aaron J. Ridley[3], Gabor Toth[3], and Roderick Heelis[4]

[1]School of Space and Environment, Beihang University, Beijing, China, [2]Space Science and Application, Los Alamos National Laboratory, Los Alamos, New Mexico, USA, [3]Department of Climate and Space Sciences, University of Michigan, Ann Arbor, Michigan, USA, [4]Department of Physics, University of Texas at Dallas, Dallas, Texas, USA

Abstract We report a self-consistent electric field coupling between the midlatitude ionospheric electrodynamics and inner magnetosphere dynamics represented in a kinetic ring current model. This implementation in the model features another self-consistency in addition to its already existing self-consistent magnetic field coupling with plasma. The model is therefore named as Ring current-Atmosphere interaction Model with Self-Consistent magnetic (*B*) and electric (*E*) fields, or RAM-SCB-E. With this new model, we explore, by comparing with previously employed empirical Weimer potential, the impact of using self-consistent electric fields on the modeling of storm time global electric potential distribution, plasma sheet particle injection, and the subauroral polarization streams (SAPS) which heavily rely on the coupled interplay between the inner magnetosphere and midlatitude ionosphere. We find the following phenomena in the self-consistent model: (1) The spatially localized enhancement of electric field is produced within $2.5 < L < 4$ during geomagnetic active time in the dusk-premidnight sector, with a similar dynamic penetration as found in statistical observations. (2) The electric potential contours show more substantial skewing toward the postmidnight than the Weimer potential, suggesting the resistance on the particles from directly injecting toward the low-*L* region. (3) The proton flux indeed indicates that the plasma sheet inner boundary at the dusk-premidnight sector is located further away from the Earth than in the Weimer potential, and a "tongue" of low-energy protons extends eastward toward the dawn, leading to the Harang reversal. (4) SAPS are reproduced in the subauroral region, and their magnitude and latitudinal width are in reasonable agreement with data.

1. Introduction

The electric field has been long considered as a crucial element in understanding the inner magnetosphere-ionosphere coupled system, owing to its important role in governing a rich variety of dynamics in the system. In the ionosphere, the electric potential pattern typically shows two convection cells, which correspond to dawn-to-dusk convection electric field over the polar cap and poleward electric field at lower latitudes. This pattern can become complex during geomagnetic disturbed conditions, including the formation of a "potential tongue" extending from premidnight to early morning sector, and an enhancement of a penetration electric field below the Region 2 current system when the current is unable to fully shield the potential from lower latitudes. It is these additions that complicate the entire coupling processes. For instance, the "tongue" usually is associated with a flow reversal, namely, the Harang reversal [*Harang*, 1946], where field-aligned currents (FACs) of opposite directions are overlap in the local time highly associated with substorm onset [e.g., *Zou et al.*, 2009; *Gkioulidou et al.*, 2009]. The penetration electric field can lead to phenomena such as ionospheric scintillation [*Kelley and Heelis*, 1989] and plasmaspheric bite outs [*Horwitz*, 1987]. Its enhancement near the dusk terminator also gives rise to increased ion drift in the ionosphere, termed subauroral polarization streams (SAPS) [*Foster and Burke*, 2002], which are closely affiliated with ring currents, FACs, electric/magnetic fields, and hot plasma dynamics in the inner magnetosphere [e.g., *Ebihara et al.*, 2009; *Wang et al.*, 2014; *Yu et al.*, 2015].

Besides the influence on the ionospheric electrodynamics, the electric field is also a primary determinant for inner magnetospheric dynamics. When the inner magnetosphere can be assumed to be free of parallel potential drop, it is reasonable to approximate the potential representing the electric field in the magnetosphere

as the same as the ionospheric potential. The convection electric field is one major element in regulating the transport of charged particles from the tail plasma sheet toward the Earth inner region [*Cao et al.*, 2011; *Zhang et al.*, 2015], providing a source population to the ring current and radiation belts. With the combined effect of magnetic gradient and curvature, charged particles drift separately eastward and westward around the Earth, with the hot ring current ions (westward drifting) carrying most of the energy content of the inner magnetosphere [*Daglis et al.*, 1999; *Daglis and Kozyra*, 2002; *Jordanova et al.*, 2012]. The same electric field also participates in the erosion of cold dense plasmaspheric particles and the formation of a drainage plume during geomagnetic active time [e.g., *Chappell et al.*, 1970; *Liu et al.*, 2015].

As described above, the electric potential along magnetic field lines acts as a bridge coupling the magnetosphere-ionosphere system. Therefore, it is important to understand not only the morphology of the electric fields but also its effects on various physical processes in the inner magnetosphere and midlatitude ionosphere. While observations of the global electric field pattern are still limited due to the limitation in the coverage of satellites in the near-Earth space, an alternative effective approach is through numerical tools. In a height-integrated ionospheric electrodynamics model, the electric field pattern is usually derived from a Poisson equation at the ionospheric altitude (e.g., ~100 km) given two major quantities $J_{||}$ and Σ:

$$\nabla \cdot (\Sigma \cdot \nabla \Phi) = -J_{||} \sin I \tag{1}$$

where $J_{||}$ is the FACs into and out of the ionosphere, Σ is the tensor of height-integrated ionospheric conductance, including both Hall and Pedersen conductances, and I is the inclination angle of the magnetic field in the ionosphere. This equation demonstrates that FACs and conductance play key roles in controlling the ionospheric electric potential/field. Although these two factors are specified at the ionosphere altitude, they are mostly determined by the magnetospheric dynamics, particularly for the Region 2 FACs [*Cao et al.*, 2008, 2010] and the midlatitude auroral conductance. The Region 2 FACs in and out of the ionosphere are diverted from the partial ring current formed during storm main phase [*Vasyliunas*, 1970]. The auroral conductance is mainly caused by keV electron precipitation that is scattered into the loss cone via wave-particle interactions in the magnetosphere [*Horne et al.*, 2003; *Ni et al.*, 2008], namely, diffuse precipitation, or accelerated down to the upper atmosphere [*Newell et al.*, 2009], namely, discrete precipitation. Therefore, the ring current evolution and plasma wave excitation are two principal regulators of the Region 2 FACs and auroral conductance. Consequently, the electric field can be generated self-consistently knowing the ring current particle distributions, which in turn feed back to the magnetospheric plasma drift, resulting in particle distributions that are used to determine the properties of plasma waves.

These relationships reveal a nonlinear feedback loop in the system and also complicate the understanding of underlying physical processes. It is a challenge for first-principle modeling studies to comprehensively and self-consistently include all the coupling processes and missing physics or inconsistent cause-effect physics in the model may introduce substantial bias. In the past decades, efforts have been extensively made to improve modeling skills, not only for a better understanding of the fundamental physics but also for a more accurate, promising predictive capability of the geospace system. One pivotal task in previous modeling efforts is to specify a realistic auroral conductance pattern because of its critical role in determining the electric field. One such specification relates the auroral conductance with FACs [e.g., *Ridley and Liemohn*, 2002; *Ridley et al.*, 2004; *Liemohn et al.*, 2004, 2005; *Ebihara et al.*, 2004; *Ilie et al.*, 2012; *Yu et al.*, 2015]. The relation was statistically derived from thousands of maps of the ionospheric Hall and Pedersen conductance and FACs generated by the assimilative mapping of ionospheric electrodynamics (AMIE) technique [*Richmond and Kamide*, 1988], described in *Ridley et al.* [2004]. It simplifies the way of prescribing the conductance and bypasses the pitfalls in embracing some direct physical processes such as diffuse auroral precipitation. While discrete auroral precipitation may be carried by FACs, diffuse precipitation caused by the wave scattering process in the magnetosphere cannot be represented by FACs. Studies also found that diffuse auroral precipitation contributes more than discrete precipitation to the energy flux deposited into the ionosphere. Another inclusive specification of auroral conductance in the inner magnetosphere models uses an empirical conductance model [e.g., *Hardy et al.*, 1987; *Galand and Richmond*, 2001; *Robinson et al.*, 1987] that calculates conductance based on precipitation flux and energy (independent on FACs) [e.g., *Fok et al.*, 2001; *Toffoletto et al.*, 2003; *Khazanov et al.*, 2003; *Chen et al.*, 2015a, 2015b; *Yu et al.*, 2016]. In most of these studies, the precipitation flux is estimated from the loss cone particle flux, which is scattered from wave-particle interactions in the inner magnetosphere. The scattering process is crudely represented by simply applying loss rates to the particles. Such rates are called lifetimes. Determining the lifetimes of charged particles at various energies is also one

popular research topic in the inner magnetosphere community [e.g., *Albert and Shprits*, 2009; *Artemyev et al.*, 2013; *Li et al.*, 2013] as it is essential for understanding the dynamics of energetic particles in both ring current and radiation belt. Recently, *Yu et al.* [2016] applied pitch angle diffusion coefficients, rather than lifetimes, to account for the wave-particle scattering processes and showed significant improvement over using a lifetime method in reproducing the measured spatial and temporal evolution of ionospheric electron precipitation. This new capability leads to a more realistic auroral precipitation pattern and is deemed to be more suitable for a physical representation of auroral conductance and for studying subauroral physics.

It should be noted that *Yu et al.* [2016] implemented such a precipitation module within a fully coupled MHD-kinetic framework, not in a stand-alone kinetic ring current model. Within that framework, the ionospheric electric potential is computed from the Poisson equation with FACs calculated in the MHD model and auroral conductance determined by the electron precipitation from the ring current model. It is known that the MHD code coupled with a kinetic ring current model produces stronger distortion of the global magnetic field owing to the inclusion of kinetic physics in the inner magnetosphere, and the Region 2 FACs at mid-latitude, deviation from the ring current, are significantly improved over pure-MHD results [*De Zeeuw et al.*, 2004]. But the Region 2 FACs are still weaker and more diffuse than observations [*Zaharia et al.*, 2006; *Yu et al.*, 2016], mainly because the ring current pressure in the MHD model is only nudged toward but does not exactly match the pressure in the kinetic ring current model. One consequence of a weaker Region 2 FAC is that the lower latitude electric field may be undershielded [*Yu et al.*, 2016] and the inner boundary of plasma sheet resides closer to the Earth. Also, the MHD grid stops at ~2.5 R_E, so low-latitude currents are not well captured in the MHD code. Therefore, in order to achieve a more realistic, fully self-consistent closure of the ring current-ionosphere coupled system, the Region 2 FACs should be simultaneously determined from the ring current dynamics rather than from MHD fields.

In this study, we utilize the newly developed physics-based and more realistic electron precipitation module in *Yu et al.* [2016] and the Region 2 FACs calculated from a stand-alone ring current model RAM-SCB (i.e., Ring current-Atmosphere interaction Model with Self-Consistent magnetic field (B)) [*Jordanova et al.*, 2006, 2010; *Zaharia et al.*, 2006, 2010] to self-consistently yield the electric field. We further investigate the global electric potential pattern, plasma sheet particle injection, and more importantly the SAPS, a physical process that is closely associated with electron precipitation and Region 2 FACs [*Foster and Burke*, 2002]. The ring current model RAM-SCB possesses a self-consistent magnetic field and computes differential particle distributions within a prescribed electric field that is usually updated from empirical electric field/potential models [e.g., *Volland*, 1973; *Stern*, 1975; *Weimer*, 2001, 2005]. The problem with these empirical electric field models is that they are not self-consistent with the first-principle calculated hot plasma dynamics. Therefore, in this study, the ring current model will be updated to calculate the electric field self-consistently, resulting in an even more self-consistent and comprehensive treatment of the plasma and fields.

2. Methodology

In this section, the kinetic ring current model RAM-SCB-E is presented in detail and the magnetic storm event under investigation is also described.

2.1. Model Description

In order to best represent the physics in the inner magnetosphere-ionosphere system, the kinetic ring current model is solved with electric/magnetic fields self-consistently determined based on the solution of the ring current phase space distribution. Figure 1 illustrates how the coupling physics is fulfilled numerically. First, the Ring current-Atmosphere interaction model (RAM) [*Jordanova et al.*, 2006, 2010] solves the Fokker-Planck equations for both ring current ions and electrons to yield their distribution functions $Q_I(R, \phi, E, \alpha)$:

$$\frac{\partial Q_I}{\partial t} + \frac{1}{R_o^2}\frac{\partial}{\partial R_o}\left(R_o^2 < \frac{\mathrm{d}R_o}{\mathrm{d}t} > Q_I\right) + \frac{\partial}{\partial \phi}\left(< \frac{\mathrm{d}\phi}{\mathrm{d}t} > Q_I\right) + \frac{1}{\gamma p}\frac{\partial}{\partial E}\left(\gamma p < \frac{\mathrm{d}E}{\mathrm{d}t} > Q_I\right) + \frac{1}{h\mu_o}\frac{\partial}{\partial \mu_o}\left(h\mu_o < \frac{\mathrm{d}\mu_o}{\mathrm{d}t} > Q_I\right) = < \left(\frac{\partial Q_I}{\partial t}\right)_{\mathrm{loss}} > \tag{2}$$

where Q_I is a function of radial distance R from 2 to 6.5 R_E with spatial resolution of 0.25 R_E, geomagnetic east longitude ϕ with resolution of 15°, energy E between 0.15 to 400 keV, and pitch angle α from 0 to 90°. The subscript I represents the species, the bracket < > represents bounce averaging, the subscript index o

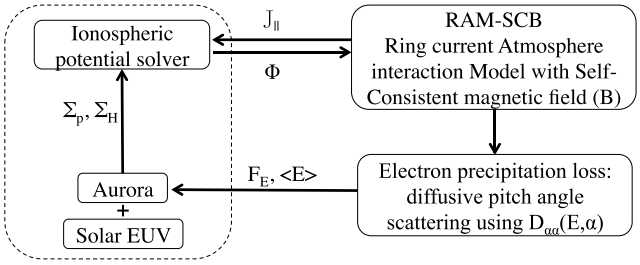

Figure 1. The coupling within the RAM-SCB-E model. The part within the dashed box is used to implement the self-consistency of electric field using inputs of $J_{||}$ and precipitation energy flux F_E from the kinetic ring current model.

denotes the magnetic equatorial plane, p is the relativistic momentum of the particle, γ is the Lorentz factor, and h is defined by:

$$h(\mu_o) = \frac{1}{2R_0}\int_{s_m}^{s'_m} \frac{ds}{\sqrt{(1 - B(s)/B_m)}} \tag{3}$$

which is proportional to the bounce period. Here B_m is the magnetic field at the mirror point, ds is a distance interval along the field line, and R_0 is the magnetic equatorial distance of the field line.

The loss terms on the right-hand side of equation (2) represent several physical processes, including charge exchange with geocoronal hydrogen for ring current ions, atmospheric collisional loss for both electrons and ions, and wave-induced scattering loss for electrons. Such scattering loss of keV electrons is induced by whistler mode chorus and hiss waves outside and inside the plasmapause, respectively, resulting in electron precipitation. This process is numerically described by a diffusion equation of the distribution function, using pitch angle diffusion coefficients obtained from statistical satellite observations [*Glauert and Horne*, 2005; *Horne et al.*, 2013; *Glauert et al.*, 2014; *Albert*, 2005]. These coefficients take into account the effect of both whistler mode chorus and hiss waves on scattering electrons from tens of eV to hundreds of keV into the loss cone. The differential electron flux within loss cones is subsequently integrated to produce the precipitation energy flux F_E (details can be found in *Yu et al.* [2016], regarding the wave-induced loss and the conversion of particle distributions at the equator to the total precipitation flux in the ionosphere).

RAM is coupled to a 3-D magnetic field equilibrium code that computes the magnetic field [*Zaharia et al.*, 2004] from the anisotropic plasma pressure provided by RAM. The resulting magnetic field in turn is used in determining the transport of charged particles and changes in their distributions [*Jordanova et al.*, 2006; *Zaharia et al.*, 2006]. This coupling is updated every 5 min.

In addition to this existing magnetic field self-consistency in the model, the electric field is also self-consistently determined at the ionospheric altitude ~100 km based on the Poisson equation (1). As the equatorial computational domain of RAM is confined within 2.0–6.5 R_E, the outermost closed magnetic field lines often find their footprints at magnetic latitudes between 70° and 60°, highly depending on the magnetospheric configuration. So while solving the electric potential in the ionosphere, the high-latitude boundary is time varying. But the low-latitude boundary is fixed at 30°. The high-latitude boundary condition is enforced by the potential calculated from the Weimer 2 K model [*Weimer*, 2001], driven by solar wind/interplanetary magnetic field (IMF) conditions and *AL* index, and the low-latitude boundary condition of potential is zero.

To solve the potential with equation (1) that takes inputs of FACs and conductance, FACs are first obtained from the Vasyliunas equation [*Vasyliunas*, 1970] that relates the field-aligned current density $J_{||}$ to the magnetic equatorial hot plasma conditions, specifically the gradient in the plasma pressure and magnetic field [*Zaharia et al.*, 2010]:

$$\mathbf{B}\cdot\nabla\left(\frac{J_{||}}{B}\right) = \frac{2\mathbf{B}\cdot(\nabla\cdot\mathbf{P}\times\kappa)}{B^2}. \tag{4}$$

where $\kappa = (\mathbf{b}\cdot\nabla\mathbf{b})$ is the field line curvature. The above equation is derived from the charge neutrality $\nabla\cdot\mathbf{J} = 0$. To obtain FACs at the ionospheric altitude, we integrate the above equation along magnetic field lines from the magnetic equator to the ionosphere.

Then, the conductance is determined from a combination of dayside conductance associated with solar radiation, and auroral conductance contributed by diffusive and discrete electron precipitation. The dayside solar

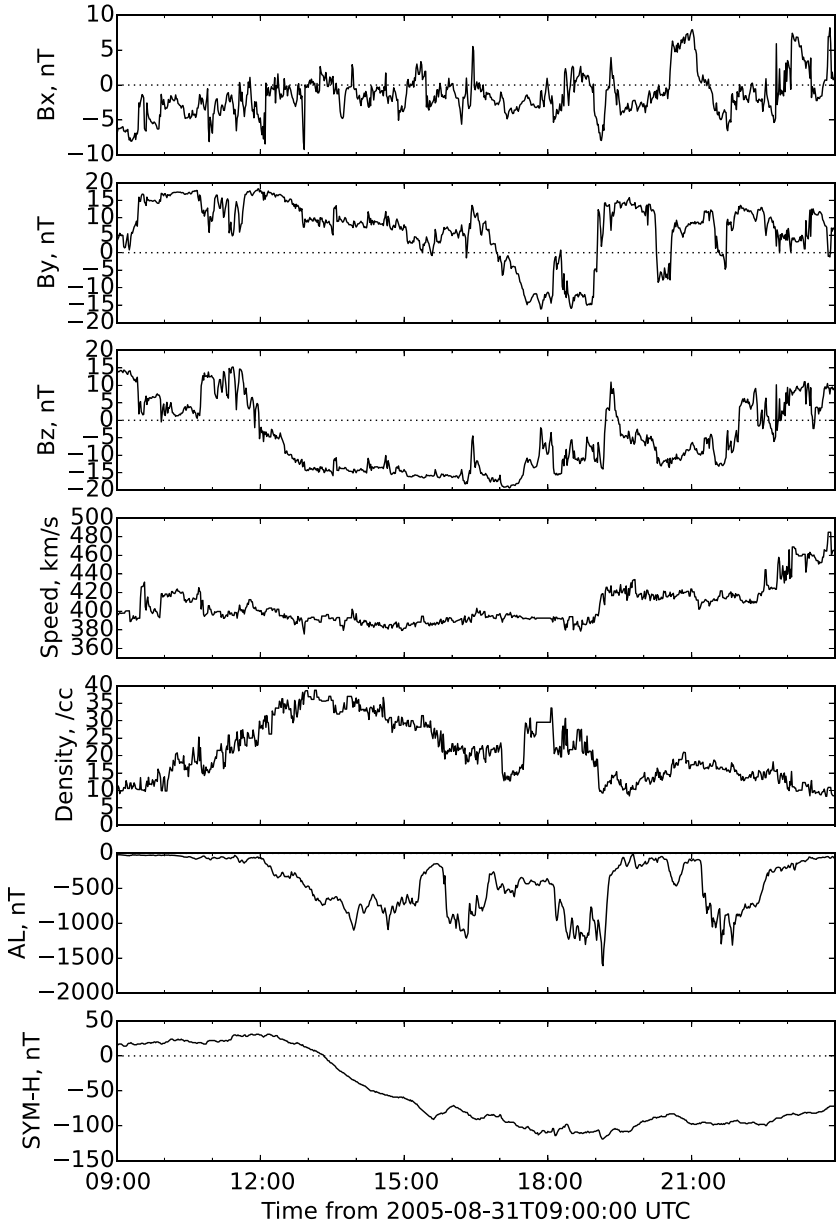

Figure 2. Solar wind and interplanetary magnetic field conditions and geomagnetic *AL* and *SYM-H* index during the storm event occurred on 31 August 2005.

EUV-induced conductance is obtained by an empirical function based on the solar zenith angle and the $F_{10.7}$ index [*Moen and Brekke*, 1993]. The auroral conductance is calculated according to the empirical Robinson relation [*Robinson et al.*, 1987] using precipitation energy flux F_E obtained from RAM as mentioned above for the diffusive aurora and using the FACs for the discrete aurora (details can be found in *Yu et al.* [2016]).

Hence, with the electric potential solved from FACs and conductance both determined by the hot plasma physics, this well coupled scheme (Figure 1) is termed RAM-SCB-E, that is, Ring current-Atmosphere interaction Model with Self-Consistent magnetic (*B*) and electric (*E*) fields.

2.2. Event Description and Model Setup

We simulate a magnetic storm event that occurred on 31 August 2005 with RAM-SCB-E. Figure 2 shows that during this event, the IMF turns southward around 12:00 UT accompanied by a large solar wind density that is sustained above 20 cm^{-3} for a few hours. The magnetic field remains southward for nearly 10 h, but the solar wind speed stays around 400 km/s. A minimum *SYM-H* index is recorded to be −120 nT at 19:00 UT

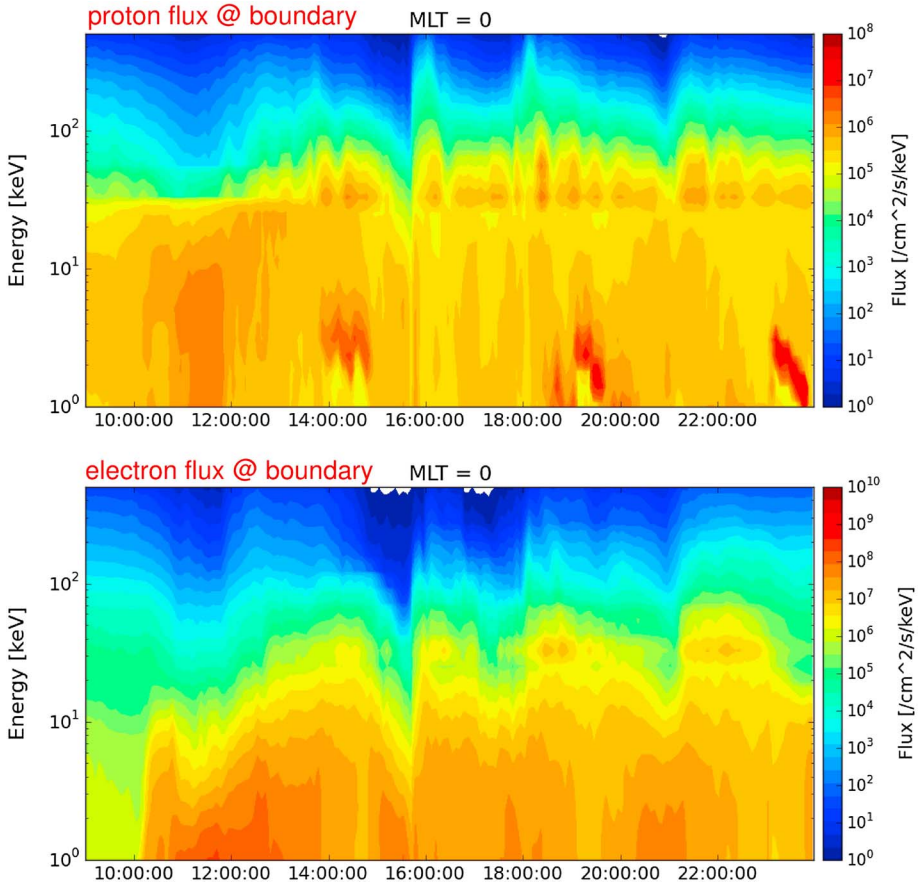

Figure 3. Particle flux obtained from LANL-geosynchronous (GEO) satellites (e.g., LANL 1989, LANL 1990, LANL 1994, LANL 1997, and LANL 2001 were available during the storm event in this study) is used to specify the boundary condition for the model at $L = 6.5$. The electron and proton fluxes at MLT = 0 are selected for demonstration.

before it gradually recovers. The *AL* index frequently hits 1000 nT. Some of these solar wind and geomagnetic conditions are used to determine the time-varying Weimer electric potential at the high-latitude boundary in the model. The plasma sheet boundary condition at $6.5R_E$ is taken from Los Alamos National Laboratory (LANL)/Synchronous Orbit Particle Analyzer (SOPA) and Magnetospheric plasma analyzer (MPA) instruments that measure electron and ion fluxes. The fluxes are then interpolated into all local times and energy grids within the model and are further decoupled into proton, helium, and oxygen ions according to *Young et al.*'s [1982] statistical results on the ratios of these ion species. Figure 3 shows such a boundary condition at MLT = 0 as an example. The low-energy proton flux is consistently high during the entire event, but the high-energy flux (above 30 keV) shows drastic injections after 12:00 UT. On the other hand, injection occurs at 10:00 UT for low-energy electrons, and similarly high-energy electrons experience continual injections in the storm main phase. These plasma sheet injections provide important sources to the ring current, as will be demonstrated in the simulation result. The magnetic field at the outer most shell of the 3-D magnetic field code is specified by the Tsyganenko magnetic field model [*Tsyganenko*, 1989] parameterized by the *Kp* index.

3. Results

Two simulations are conducted for the storm event: one uses a self-consistent electric field as described above and the other one uses a prescribed electric potential model [i.e., *Weimer*, 2001] in governing the ring current particle transport. The latter, based on statistical observations, cannot represent the feedback effects of the changes in the hot populations on the ionospheric electrodynamics in this particular simulation. That is, the part inside the dashed rectangle in Figure 1 is not represented in the simulation. By comparing these two types of simulation, we intend to address the following questions: How different is the self-consistent electric field

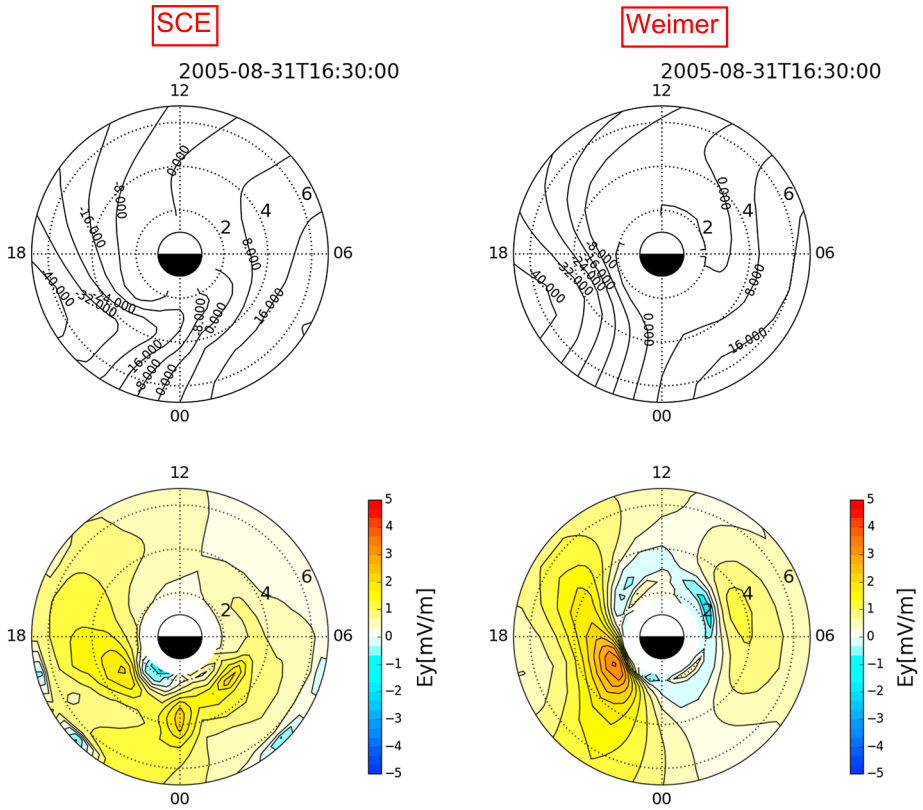

Figure 4. (top row) Magnetic equatorial potential pattern and (bottom row) the *Y* component of the convection electric field in (left column) the self-consistent electric field method and (right column) Weimer potential model. The dashed circles in each plot indicates L shells at 2, 4, and 6 respectively.

from empirically obtained representation? What are the influences on inner magnetosphere drift physics? What are the influences on ionospheric electrodynamics?

3.1. Effect on the Inner Magnetospheric Dynamics

Figure 4 illustrates electric potential contours and dawn-to-dusk convection electric fields (E_y) mapped from the ionospheric altitude where the potential is solved with equation (1) during the storm main phase for both simulations. Two main features are distinctive: (1) The potential contour lines from the self-consistent solver show stronger skewing in the dusk-to-postmidnight sector than the Weimer potential contours and (2) the Weimer model shows a much stronger dawn-to-dusk electric field (E_y) in the dusk sector than in the self-consistent case. While the potential contour skewing may suggest an effect from the transport of energetic particles, the localized electric field enhancement indicates the degree of penetration of the convection.

It is also known that the potential contour skewing is associated with inner magnetosphere shielding that prevents the convection electric field in the outer magnetosphere from penetrating into the inner region. The above difference in the potential patterns suggests that the Weimer potential is less shielded than the self-consistent potential, because the latter experiences a weaker penetration field. To demonstrate the penetration and shielding effects during the entire storm event, Figure 5 shows the dawn-to-dusk component of convection electric field (E_y) at MLT = 20, as a function of radial distance and UT time. Localized enhancements of penetration electric field are evident in both cases but with remarkable differences. The self-consistent solver displays gradual migration of the peak of the penetration electric field, with the electric field well shielded in the prestorm time at 12:00 UT, and then penetrating from $L = 4.5$ to 3.0 during storm main phase until retreating back to $L = 4$ in the early recovery phase. Such a process precisely implies the competition between the establishment of Region 2 FACs, ionospheric currents, and changes in the convection strength. While changes in the convection that respond with a longer time scale than the currents may be effectively shielded, sudden transitions like the IMF southward turning can lead to a rapid increase in the polar cap

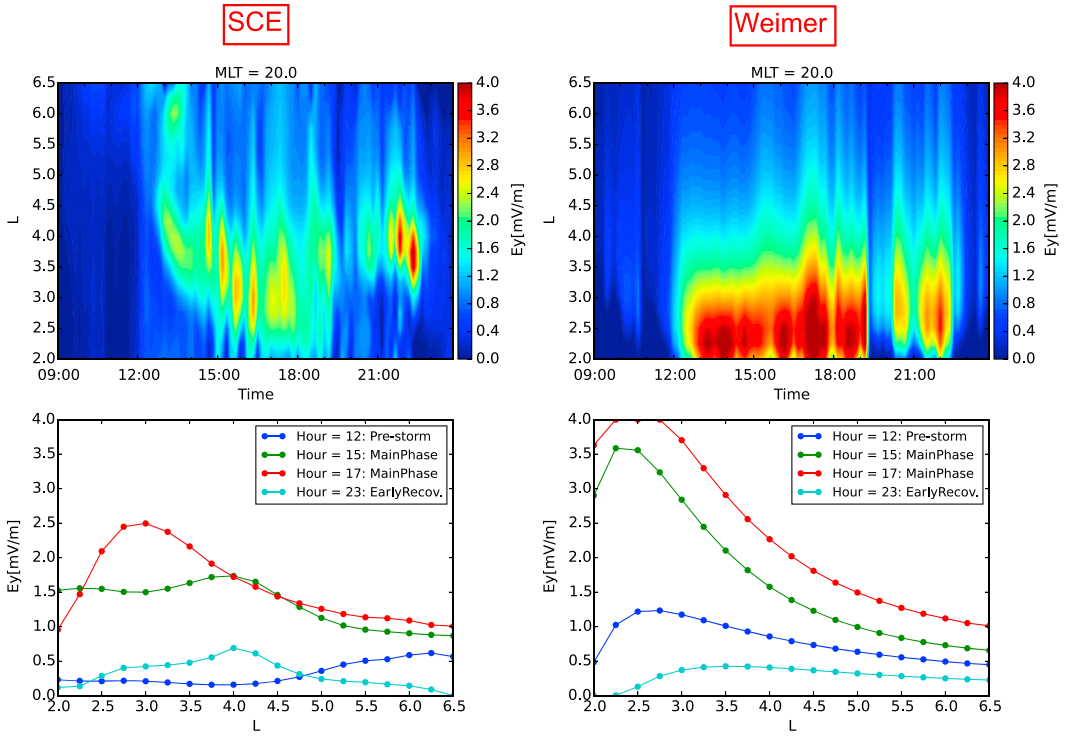

Figure 5. Dawn-to-dusk convection electric field component at MLT = 20 in the (left column) self-consistent electric field approach and (right column) Weimer model. (top row) Electric field as a function of L and UT; (bottom row) electric field as a function of L at four selected times, covering from prestorm, storm main phase, and recovery phase.

potential, causing large penetration of the convection electric field. But meanwhile the formation and enhancement of ring current, FACs, and ionospheric currents create a shielding electric field in the ionosphere (Region 2 FACs are connected with dusk-to-dawn Pedersen current in the nightside sector), opposing the penetration and resulting in a "residual" dawn-to-dusk convection electric field in the undershielded situation.

In contrast, with a Weimer potential model, since the FACs and ionospheric currents do not respond self-consistently to oppose the dawn-to-dusk convection electric field, the penetration electric field is much greater and extends to lower L shells, even during prestorm time. The peak of the penetration electric field is located around $L = 2.5$ or even closer, regardless of the storm phase. The gradual inward motion of the penetration along with the development of the ring current is not present, indicating a nonself-consistent response between the ring current, FACs, ionospheric current, and the prescribed electric field.

The radially localized enhancement of the penetration electric field has been statistically studied using satellite observations [e.g., *Rowland and Wygant*, 1998; *Nishimura et al.*, 2006, 2007; *Matsui et al.*, 2004, 2013] for different geomagnetic activity levels. The observational studies show that the dawn-to-dusk electric field in the dusk sector of the inner magnetosphere usually increases with radial distance under quiet and less disturbed conditions, but a localized peak of the electric field appears around $L = 3–4$ for disturbed time and moves outward during storm recovery phase. In agreement with the observational results, our simulation with a self-consistent electric field produces a similar dynamic electric field penetration that varies with the evolution of the ring current. This approach therefore shows a more reasonable and consistent picture of the radial distribution of the dawn-to-dusk electric field.

To examine the effect of the potential pattern on particle transport, we next study the particle injections from the outer boundary. When particles travel through the inner magnetosphere, they experience various electric and magnetic drifts induced by the perpendicular electric field and the gradient and curvature of the magnetic field. The electric potential contours represent the drift trajectory of zero-energy particles, while higher-energy particles are more subject to magnetic gradient and curvature drift. From the electric potential pattern across midnight in Figure 4, we expect to see a diverted flow of low-energy protons in the simulation with a self-consistent electric field and direct injection in the simulation with the Weimer model.

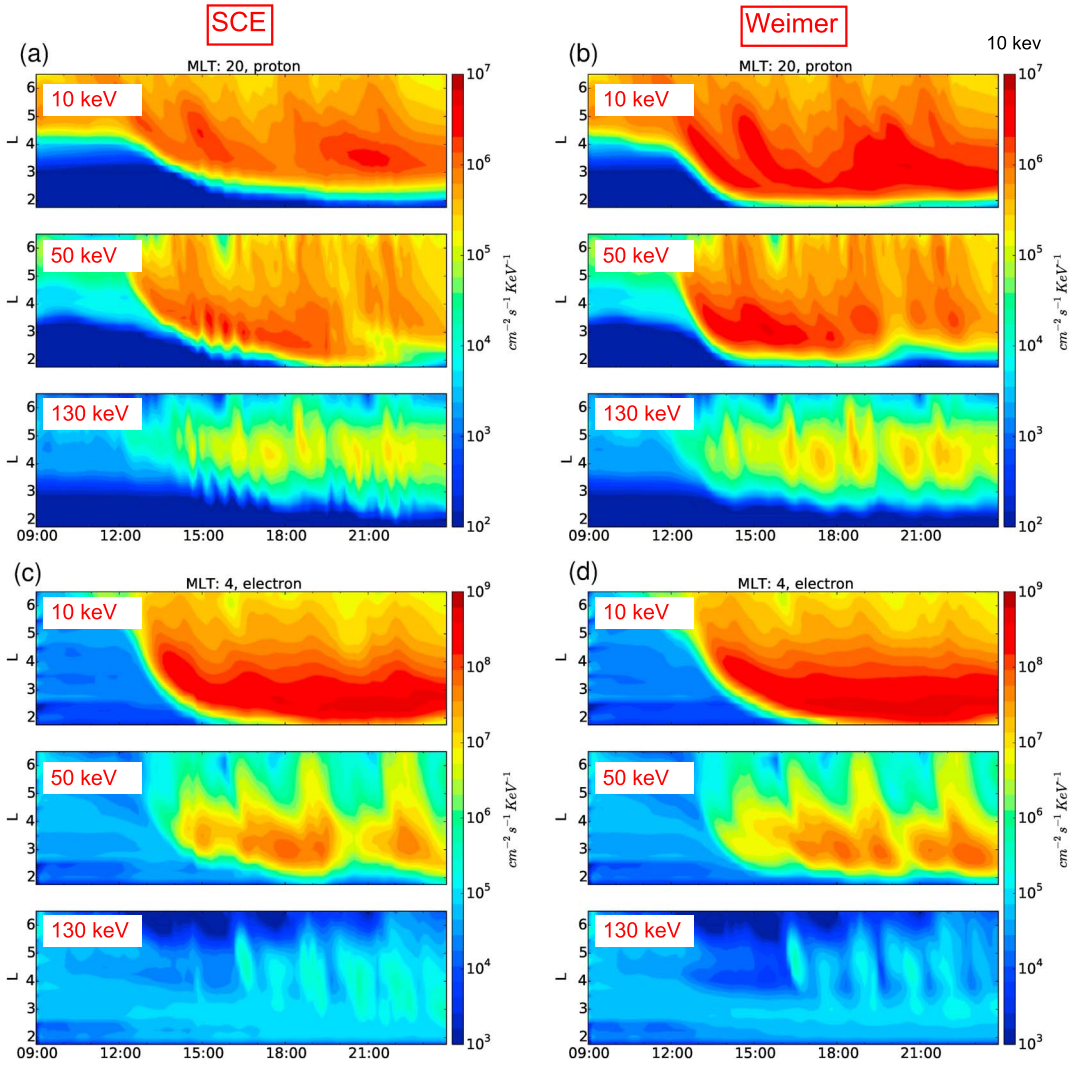

Figure 6. Ring current proton and electron flux as function of L shell and time selected at MLT = 20 for protons and MLT = 4 for electrons. (a and c) Use self-consistent electric field model. (b and d) Use Weimer electric potential model. During the storm main phase, low-energy protons are convected toward the Earth with the aid of convection electric field. The Weimer potential model shows more profound effect on the low-energy plasma transport as they penetrate well deep down to 2.0 R_E, but they are nearly prohibited at 2.5 R_E when a self-consistent electric field model is used. For high-energy protons and electrons in various energy, their inward transport is similar in both simulations.

Indeed, Figure 6 illustrates that under the influence of a self-consistent electric field (Figure 6a, top), protons at $E = 9.3$ keV in the dusk-premidnight sector are convected inward from the outer boundary and their flux significantly drops near $L = 2.5$. In contrast, these low-energy protons maintain high-level flux down to $L = 2$ and eventually get lost from the inner boundary when the Weimer electric field is utilized (Figure 6b, top). At higher energies, the proton injections from the outer boundary down to the inner region behave similarly in both cases, so do the electrons in the early morning sector (Figures 6c and 6d). This similarity in the electron dynamics is probably attributed to the similar electric potential contours and magnetic field configuration in the dawn sector.

Although high-energy protons above 30 keV are the dominant contributor to the ring current energy and carry most of the energy content of the inner magnetosphere, low-energy ions are of particular importance to the premidnight electrodynamics, especially in the Harang reversal commonly detected in the ionosphere. *Gkioulidou et al.* [2009] conducted detailed analysis of the Rice Convection Model (RCM) simulation and found that a pair of FACs with opposite polarity overlaps near the same midnight local time across different latitudes is necessary for the formation of the Harang reversal. Such a pair of FACs (downward and upward) is found to

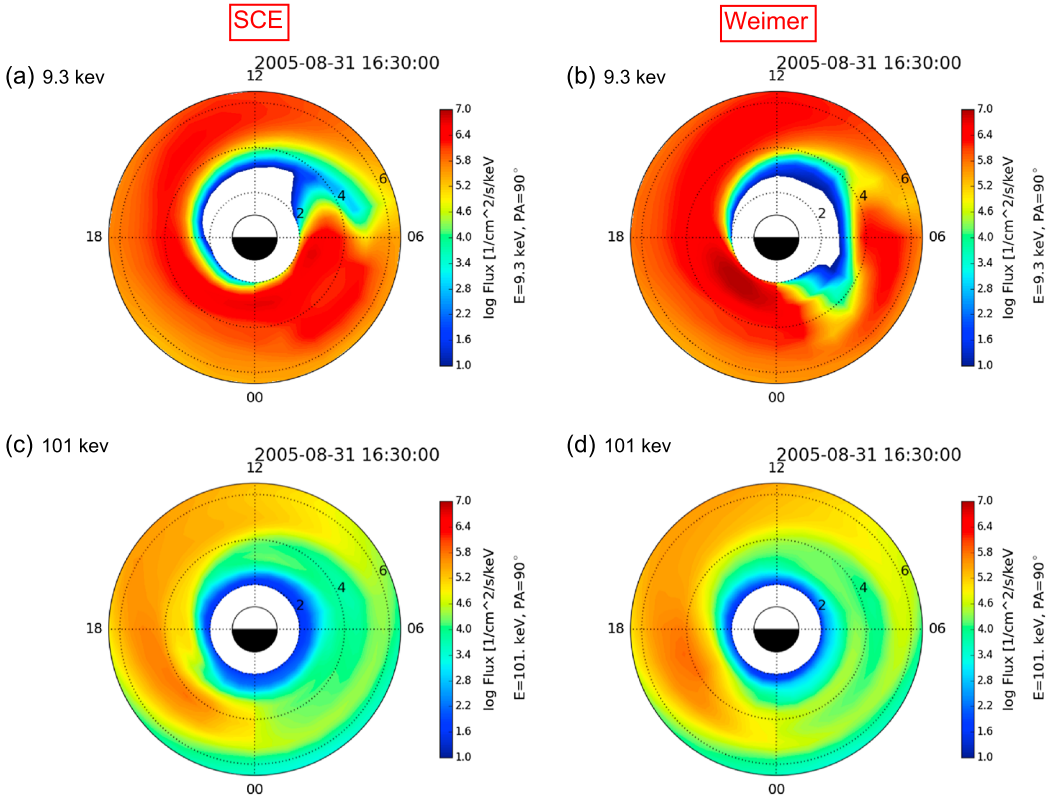

Figure 7. Ring current proton flux at (a and b) 9.3 keV and (c and d) 100 keV with pitch angle near 90°. In the case with self-consistent electric field, low-energy protons are convected from dusk to dawn through midnight, affected by the potential contours that are skewed toward early morning sector as shown in Figure 4. On the contrary, under the prescribed Weimer potential, low-energy protons preferentially convect toward dayside mainly through the duskside. The high-energy proton fluxes are similar in both cases.

be associated with low-energy ions penetrating closer to the Earth toward the dawnside and high-energy ions that are further away from the Earth. In this study, the simulation with a self-consistent electric field presents a tongue of 9.3 keV protons extending across midnight toward dawn in the low L shell region, as shown in Figure 7, but limited extension is developed in the Weimer case. On the other hand, the high-energy protons in both cases do not extend towards the dawn or penetrate as deeply as the low-energy protons. Such an extension of low-energy protons in wider MLT coverage, as concluded in *Gkioulidou et al.* [2009], is highly related to the downward FACs into the ionosphere, which can control the ionospheric electrodynamics to be discussed in the next section. In contrast, the Weimer electric potential does not interact with the real-time FACs originating from the inner magnetosphere.

3.2. Effect on the Ionospheric Electrodynamics

Figure 8a displays the FACs at the ionospheric altitudes calculated from the ring current. As expected, downward FACs in the duskside extend across local midnight toward the dawnside, equatorward of the upward FACs. An MLT overlap region is formed near midnight, allowing for the formation of the Harang reversal [*Gkioulidou et al.*, 2009]. Figure 8b presents the conductance contributed from a combination of solar irradiance and auroral precipitation originating from the wave-induced pitch angle scattering of ring current electrons. An enhanced auroral conductance is evident around 60° in the premidnight to the dawn sector as the chorus waves responsible for the electron scattering are mostly active in that region. From FACs and conductance, the self-consistent electric potential is generated (Figure 8c). A tongue of the negative potential cell (potential well) in the duskside stretches into early morning at low latitudes, representing the Harang reversal. The westward return flows in the reversal at lower latitudes are located on top of the collapsed potential contour lines (i.e., a large potential gradient or electric field) where conductance is low, resulting in enhanced flow speed, or SAPS, shown in Figure 8d. The speed exceeds 1000 m/s around latitude of 55° in the dusk-to-premidnight sector, a typical location reported from observations. By contrast, the Weimer potential pattern

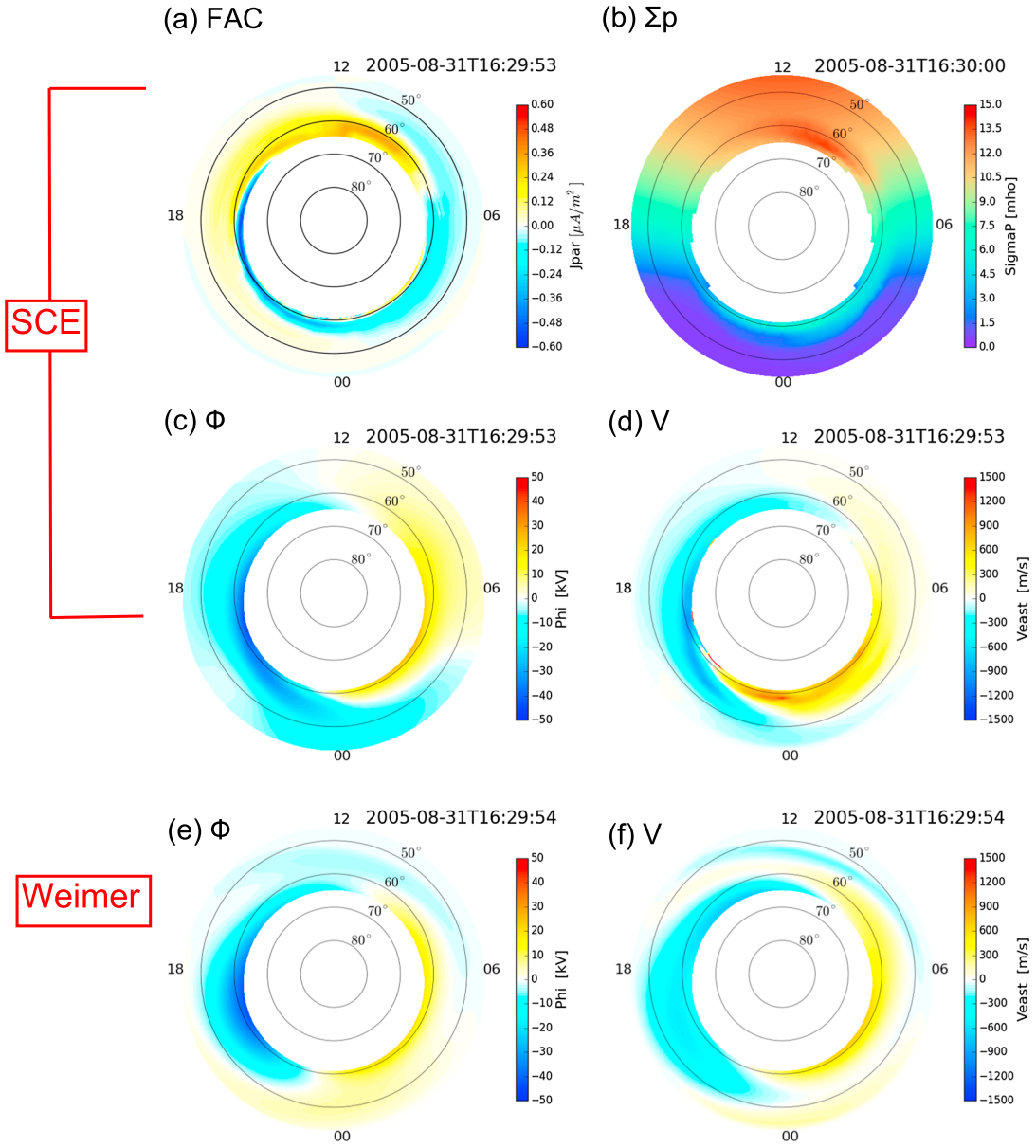

Figure 8. Global pattern of (a) ionospheric FACs, (b) Pedersen conductance, (c and e) electric potential, and (d and f) eastward flow in the ionosphere altitude from simulations with either both self-consistent (Figures 8a–8d) or Weimer (Figures 8e and 8f) electric field.

(Figures 8e and 8f) has neither extension of the negative cell nor sharp gradient, meaning that SAPS are not prominent.

To verify that the flow in the self-consistent simulation is indeed SAPS, the subauroral region is first identified. It is defined as a region located below the equatorward edge of auroral precipitation. Figure 9d shows the auroral precipitation energy flux at MLT = 21 as a function of latitude. A rapid drop of the precipitation energy flux marks the equatorward edge of the auroral boundary, denoted by the vertical dashed line. In the subauroral region, the precipitation flux is about 3 orders of magnitude lower, and the conductance falls to 0.5 mhos. The downward Region 2 FACs flow into this subauroral region, and a strong poleward electric field is produced in order to drive the horizontal Pedersen current that connects to the upward Region 1 FACs at higher latitudes. This leads to an enhancement of westward flows in the subauroral region, namely, SAPS at ~55° latitude. As a flow speed above 500 m/s in the subauroral region is commonly referred as SAPS, it is found that SAPS occur in the region equatorward of the enhanced Pedersen conductance and concurrent with both Regions 1 and 2 FACs. The SAPS peak is located between the peaks of Region 1 and Region 2 FACs with the

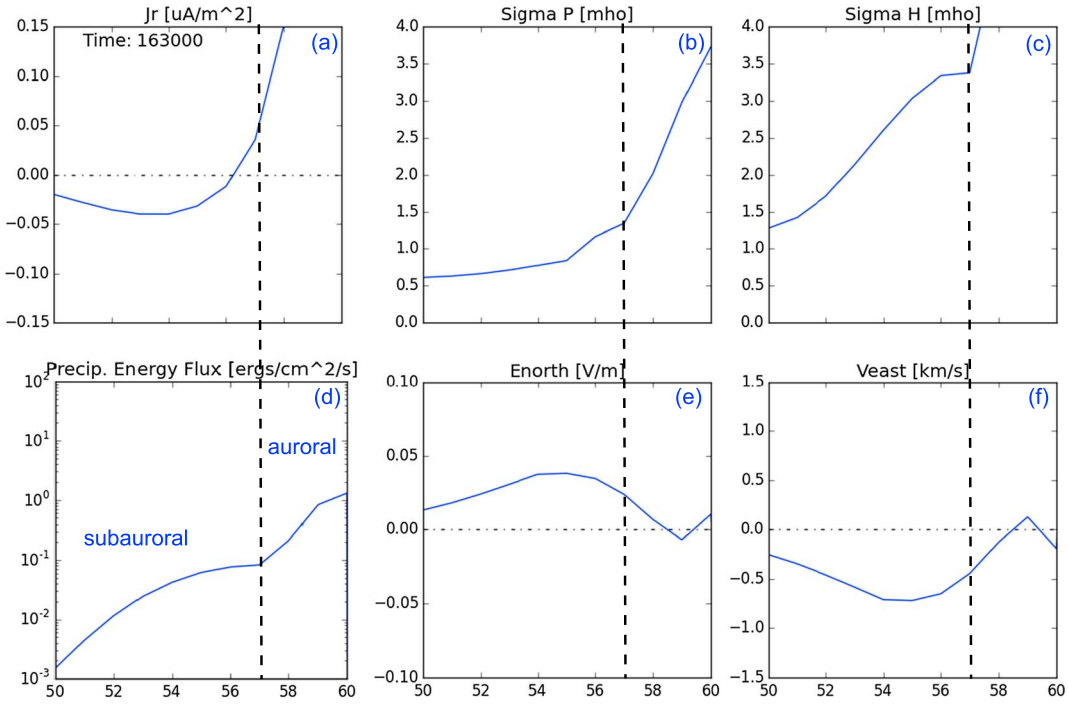

Figure 9. Simulation results from using self-consistent electric field: latitudinal distribution of FACs, Pedersen and Hall conductance, precipitated electron energy flux, poleward electric field, and eastward drift velocity at the ionospheric altitude for MLT = 21. The vertical dashed line denotes the equatorward boundary of auroral precipitation, where precipitation is significantly lower in the subauroral region than in the auroral latitudes.

Region 2 FAC well below the equatorward edge of the auroral boundary. These relative positions are in agreement with statistical observational results reported in *Wang et al.* [2014] and reveal relationships consistent with the current-generator mechanism proposed in *Anderson et al.* [1991, 2001].

Figure 10 shows simulation results extracted along two consecutive DMSP trajectories in the subauroral region in the dusk-premidnight sector when the satellite flew across the polar cap region approximately from 21:00 MLT toward 09:00 MLT in the Northern Hemisphere. Due to the cutoff at the high-latitude boundary, the model only shows results at midlatitudes which, however, sufficiently describe the subauroral dynamics. Along the first orbit, the spacecraft first measures a negative sunward flow, peaking around the latitude of 52°, and decreases with increasing latitude. It then detects an increase of flow speed again above 60°, which is the auroral zone flow at higher latitude. Such a trend is well captured by the simulation (blue line), which shows a comparable magnitude for the SAPS. The observed peak of SAPS, however, appears at lower latitudes by 2–3°, and flow channel is narrower. In the second orbit, the model reproduces a comparable width of the flow channel, which again misses the observed peak flow by 2–3° toward higher latitudes.

In the bottom panels, the Pedersen conductance is compared. The Pedersen conductance based on observations is computed from both electron and ion precipitation measured by the DMSP spacecraft. The electron associated conductance is computed from the Robinson relation [*Robinson et al.*, 1987] (black dashed line), while the ion associated (mainly protons) conductance is from the Galand and Richmond relation [*Galand and Richmond*, 2001]. Both relations take into account the precipitation energy flux and averaged energy. It can be clearly seen during the first orbit that the proton precipitation significantly contributes to the auroral conductance below the equatorward edge of the electron precipitation boundary, although the second orbit shows a much smaller contribution near that region. Such a difference is attributed to the time-varying separation between the inner boundaries of the ion and electron plasma sheets. During the second orbit, the separation is not very clear, probably owing to a weaker electric potential at that time. Nevertheless, between these two inner boundaries, the ion precipitation cannot be neglected given that it significantly enhances the auroral conductance near the equatorward edge of the auroral boundary. In the simulation, the conductance rapidly increases near the equatorward boundary of the observed electron auroral zone, but the magnitude is underestimated. This may be caused by an inadequate precipitation flux into to the ionosphere. It is possible

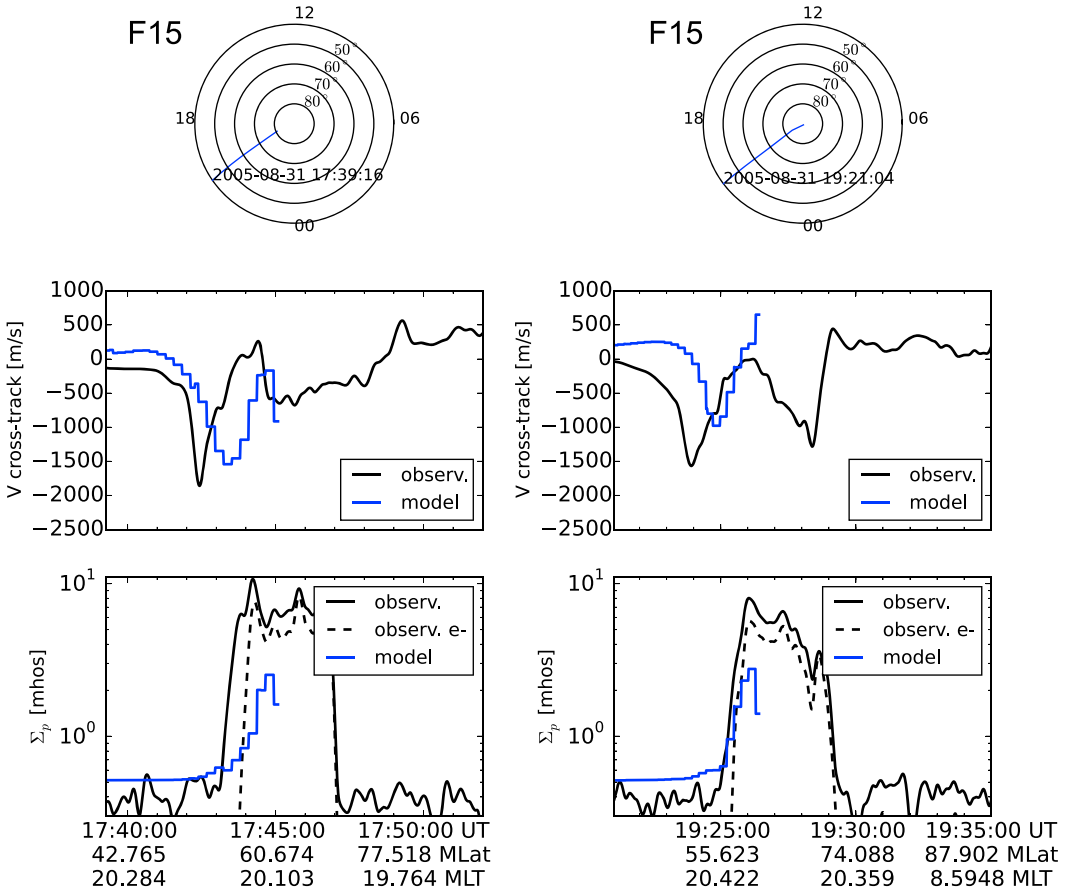

Figure 10. Comparisons of flow speed and Pedersen conductance between the self-consistent simulation (blue) and DMSP measurements (black). All passes are in the Northern Hemisphere, flying from the duskside to dawnside. Negative cross-track flow represents a westward velocity to the left of the trajectory direction. The Pedersen conductance based on observations is calculated from the measured precipitation flux (here the solid black line marks the conductance associated with both electron and ion precipitation, and the dashed black line denotes that only from electron precipitation).

that the statistical averaged pitch angle diffusion coefficients used to account for electron loss are not strong enough or representative in this intense storm event, or that whistler mode waves are not the only driver of diffuse electron precipitation, or that the electron energy distributions can be altered during the precipitation process from the magnetosphere to the ionosphere, so the integrated precipitation energy flux at the ionospheric altitude is larger than that in the magnetospheric source region. It should also be noted that the ion precipitation is not yet incorporated into the model, which might be an additional cause of the underestimation. Our future study will add ion precipitation caused by magnetic field line curvature scattering and electromagnetic ion cyclotron waves and further examine their relative importance in the ionospheric electrodynamics.

4. Discussion

In the above comparisons, we noticed that although the magnitude and width of the SAPS channel produced by RAM-SCB-E are in reasonable agreement with the data, they appear at slightly higher latitudes than observed. This is probably associated with a weaker representation of the ring current in the simulation. Figure 11 shows the simulated *Dst* index, calculated with the Dessler-Parker-Sckopke relationship [*Dessler and Parker*, 1959; *Sckopke*, 1966] from the content of ring current energy. It is not as strong as the measured *SYM-H* index. A weaker ring current creates a more dipolar magnetic field configuration in which the footprints of the magnetic field lines lie at higher latitudes than in reality. The underestimation of ring current may be associated with the boundary conditions of plasma sheet flux that were not realistically specified over all local times, because the flux at 24 local times are interpolated from three well-separated geosynchronous LANL

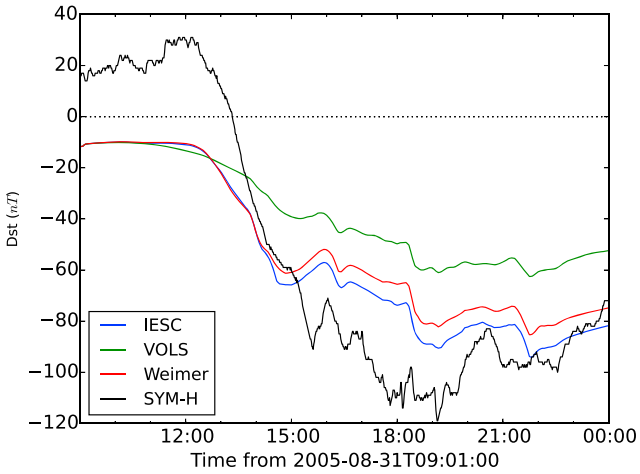

Figure 11. Measured *SYM-H* index (black) and simulated *Dst* index using different electric field models. "IESC" stands for self-consistent electric field, "VOLS" is for Volland-Stern electric field, and "Weimer" uses Weimer potential model.

satellites in this simulation. This may lead to underestimated plasma sheet sources convecting from the tail into the inner magnetosphere, creating a ring current with smaller strength. Indeed, during the storm main phase, these three satellites are located from postmidnight to the dayside, corotating eastward, missing the important source region in the dusk-midnight sector. This means that highly possible localized injections in that region are not captured by these satellites nor included in the simulation, which is likely the reason of underestimation. We conducted an experiment that increases the boundary flux by a factor of 1.5 and found that the ring current, as expected, is enhanced and the *Dst* index is closer to the observation. However, the position of Region 2 FACs flowing into the ionosphere in the subauroral region is not greatly changed, probably because the nondipolar configuration in the inner region is not significantly altered. Thus, the boundary condition does not seem to be the direct or only cause of the mismatch of the SAPS peak. It should be noted that the tail current and other induced currents on ground may also contribute to the *SYM-H* index during storm main phase. If that compensates the simulated *Dst* index, the ring current is actually not significantly underestimated. Therefore, other causes should be sought for the offsetting of the position of SAPS. Nevertheless, inadequate specification of the outer boundary potential may be an improvement that requires further attention.

We then propose another possibility that causes the location of SAPS appearing at higher latitude. It may lie in the location of precipitation since the equatorward edge of the electron precipitation is closely related to the location of the SAPS peak. To capture the right position of the SAPS, a better representation of the auroral precipitation is another critical element. We also notice from the data that the ion precipitation actually contributes significantly to the auroral conductance, particularly below the equatorward edge of the electron precipitation. This contributes to an additional enhancement of conductance equatorward of the electron aurora. Yet in the simulation, not only the ion precipitation is missing but also the electron precipitation is insufficiently included. These combined effects may contribute to the underestimation in the conductance and the deviation of the location of SAPS. We performed an experiment that shifts the equatorward edge of the aurora (i.e., maps the precipitation flux) toward lower latitudes by 2° and found the peak of SAPS appearing at lower latitudes, consistent with the observations. Such an experiment suggests the importance of a correct location of the equatorward edge of auroral precipitation, which might be complemented by the ion precipitation. The implementation of such ion precipitation will be our next research task.

In revealing the SAPS features, we are aware that observations often reported that SAPS are well separated from the high-latitude auroral returning flow in the same westward direction, thus featured a "double-dip" profile in the velocity [*Foster and Burke*, 2002]. The spatial separation is small but varies from 1° to a few degrees. In our simulation, due to the limited coverage of the simulation domain, the high-latitude auroral region is not fully resolved by the model, and the high-latitude westward flow is not well produced in the storm main phase as shown in Figure 8. Nevertheless, during early storm main phase (e.g., around 13–14 UT) when the high-latitude boundary of the ionospheric solver is still around 65° in the dusk-to-premidnight sector due to less stretched magnetic field configuration, the auroral returning flow is captured above 60°, forming two westward flows around MLT from 19 to 22, hence consistent with observations.

Regarding the finite width of the SAPS channel, we expect a finer resolution of the model may sharpen the narrow-scale features. The current spatial resolution of 0.25 R_E in the equatorial plane corresponds to a spatial separation of 1° around magnetic latitude of 60°, and 2.5° separation around magnetic latitude of 50°. Such a model resolution may smear out small-scale fluctuations in the electric field or velocity, leading to

averaged results. A finer resolution thus is in demand in the future for a better performance of resolving small-scale features.

5. Summary

This study investigated the effects of using a self-consistent treatment of electric field in the kinetic ring current model on the hot plasma dynamics and electrodynamics especially in the midlatitude ionosphere. The ring current model thus includes both electric and magnetic field self-consistency and is named RAM-SCB-E. The new model uses a recently developed, physics-based electron precipitation module that accounts for the diffusive pitch angle scattering processes caused by whistler waves by using pitch angle-dependent diffusion coefficients. Such a module gives rise to a more realistic temporal and spatial distribution of electron precipitation [*Yu et al.*, 2016] and provides a more realistic auroral precipitation pattern needed in specifying the ionospheric conductance in the model. While *Yu et al.* [2016] used this module in a coupled framework in which the ring current model is coupled to an MHD code, this study only treats the ring current model in a stand-alone fashion. It is a big advancement from the previous stand-alone version of the ring current model using empirical electric fields that omit the feedback effect of the hot plasma physics on the large-scale convection electric field.

Two simulations are performed using either a self-consistent electric field or the empirical Weimer potential. Significant differences are found, especially in the transport of low-energy protons and the electrodynamics that are closely associated with the coupling between the inner magnetosphere and the midlatitude ionospheric region. It is these dynamics that play an important role in controlling the coupling processes and emphasize the necessity of modeling the system in a self-consistent manner to account for the complicated interactions within it.

When comparing these two approaches, we found the following results:

1. RAM-SCB-E produces local enhancements of penetration electric field in the dusk-premidnight sector, the peak of which gradually evolves to lower L shells as the ring current is being built up, whereas the empirical model produces a larger and more stable penetration electric field inside $L = 3$ during the entire storm event. The former is thus in better agreement with statistical results reported in *Rowland and Wygant* [1998], which showed that the spatial distribution of the local electric field enhancement in the dusk sector depends on the geomagnetic activity level.
2. The electric potential pattern in the magnetic equatorial plane shows more predominant skewing in the dusk-premidnight sector around $L = 4$ in the self-consistent case than in the empirical model case, causing more shielding from the outer region. The low-energy protons are thus transported along different paths rather than directly along the Sun-Earth direction. They are diverted azimuthally eastward and cannot reach the deep inner magnetosphere in the dusk-midnight sector as they do under the Weimer potential. For high-energy protons and electrons, no significant difference is found.
3. Since the low-energy protons are associated with FACs in the midlatitude [*Gkioulidou et al.*, 2009], they are closely related to the midlatitude electrodynamics, which reflects the feedback effect within the coupled system. We found that the eastward extending FACs in the midlatitudes induce the Harang reversal that is missing in the Weimer model.
4. Another outstanding feature in the subauroral region is that subauroral polarization streams (SAPS) are captured when using a self-consistent electric field but are not distinguished in the empirical model. RAM-SCB-E also verifies the popular current-generator mechanism for SAPS, which are proposed to be generated when FACs flow into the subauroral ionosphere where the conductance is relatively low with respect to the auroral zone.

Besides the above results, we realize that even more self-consistent physics is further needed in order to understand the underlying processes more precisely. In this study, albeit with the physics-based precipitation flux down to the ionospheric altitude, the calculation of auroral conductance still relies on the empirical Robinson formalism under an assumption of Maxwellian distribution. Removing this empirical limitation is currently in progress, typically by coupling the inner magnetosphere model with an upper atmosphere model, which, given the auroral precipitation flux, determines the vertical ionization profile and thus the ionospheric conductivity. This will establish a truly self-consistent midlatitude ionospheric electrodynamics with the inner magnetosphere. Recently, one such effort was reported in *Huba and Sazykin* [2014]; *Huba et al.* [2017] that coupled the global ionosphere-plasmasphere model SAMI3 with the ring current model RCM and demonstrated

the underlying processes within the ionosphere-plasmasphere-ring current system. These studies not only revealed the power of self-consistent modeling of fundamental physics but also initiated the direction to more comprehensively accounting for the coupled system.

Acknowledgments
The authors thank the OMNIweb from NASA Goddard Space Flight Center for providing the solar wind/interplanetary field data and the Kyoto, Japan World Data Center System for providing the *SYM-H* index and *AE* index. The DMSP particle detectors were designed by Dave Hardy of AFRL, and the data are obtained from JHU/APL. This work was supported by the NSFC grants 41574156 and 41431071, by the Fundamental Research Funds for the Central Universities, by the Special Program for Applied Research on Super Computation of the NSFC-Guangdong Joint Fund, and by the Chinese Program for Thousands Young Talents. The work at LANL was conducted under the auspices of the U.S. Department of Energy, with partial support from the Los Alamos National Laboratory Directed Research and Development (LDRD) program under contract DE-AC52-06NA25396. Part of these simulations was performed on TianHe-2 at National Supercomputer Center in Guangzhou, China. Data used in the study will be made available upon request by contacting the corresponding author.

References

Albert, J., and Y. Shprits (2009), Estimates of lifetimes against pitch angle diffusion, *J. Atmos. Sol. Terr. Phys.*, *71*(16), 1647–1652, doi:10.1016/j.jastp.2008.07.004.

Albert, J. M. (2005), Evaluation of quasi-linear diffusion coefficients for whistler mode waves in a plasma with arbitrary density ratio, *J. Geophys. Res.*, *110*, A03218, doi:10.1029/2004JA010844.

Anderson, P. C., R. A. Heelis, and W. B. Hanson (1991), The ionospheric signatures of rapid subauroral ion drifts, *J. Geophys. Res.*, *96*(A4), 5785–5792, doi:10.1029/90JA02651.

Anderson, P. C., D. L. Carpenter, K. Tsuruda, T. Mukai, and F. J. Rich (2001), Multisatellite observations of rapid subauroral ion drifts (SAID), *J. Geophys. Res.*, *106*(A12), 29,585–29,599, doi:10.1029/2001JA000128.

Artemyev, A. V., D. Mourenas, O. V. Agapitov, and V. V. Krasnoselskikh (2013), Parametric validations of analytical lifetime estimates for radiation belt electron diffusion by whistler waves, *Ann. Geophys.*, *31*, 599–624, doi:10.5194/angeo-31-599-2013.

Cao, J., et al. (2008), Characteristics of middle- to low-latitude Pi2 excited by bursty bulk flows, *J. Geophys. Res. Atmos.*, *113*(A7), 521–532.

Cao, J. B., et al. (2010), Geomagnetic signatures of current wedge produced by fast flows in a plasma sheet, *J. Geophys. Res.*, *115*, A08205, doi:10.1029/2009JA014891.

Cao, J. B., W. Z. Ding, H. Reme, I. Dandouras, M. Dunlop, Z. X. Liu, and J. Y. Yang (2011), The statistical studies of the inner boundary of plasma sheet, *Ann. Geophys.*, *29*(2), 289–298, doi:10.5194/angeo-29-289-2011.

Chappell, C. R., K. K. Harris, and G. W. Sharp (1970), The morphology of the bulge region of the plasmasphere, *J. Geophys. Res. Atmos.*, *75*(75), 3848–3861.

Chen, M. W., C. L. Lemon, T. B. Guild, A. M. Keesee, A. Lui, J. Goldstein, J. V. Rodriguez, and P. C. Anderson (2015a), Effects of modeled ionospheric conductance and electron loss on self-consistent ring current simulations during the 5–7 April 2010 storm, *J. Geophys. Res. Space Physics*, *120*, doi:10.1002/2015JA021285.

Chen, M. W., C. L. Lemon, K. Orlova, Y. Shprits, J. Hecht, and R. L. Walterscheid (2015b), Comparison of simulated and observed trapped and precipitating electron fluxes during a magnetic storm, *Geophys. Res. Lett.*, *42*, 8302–8311, doi:10.1002/2015GL065737.

Daglis, I., and J. Kozyra (2002), Outstanding issues of ring current dynamics, *J. Atmos. Sol. Terr. Phys.*, *64*(2), 253–264, doi:10.1016/S1364-6826(01)00087-6.

Daglis, I. A., R. M. Thorne, B. Wolfgang, and O. Stefano (1999), The terrestrial ring current: Origin, formation, and decay, *Rev. Geophys.*, *37*(4), 407–438.

De Zeeuw, D. L., S. Sazykin, R. A. Wolf, T. I. Gombosi, A. J. Ridley, and G. Tóth (2004), Coupling of a global MHD code and an inner magnetospheric model: Initial results, *J. Geophys. Res.*, *109*, A12219, doi:10.1029/2003JA010366.

Dessler, A. J., and E. N. Parker (1959), Hydromagnetic theory of geomagnetic storms, *J. Geophys. Res.*, *64*, 2239–2252, doi:10.1029/JZ064i012p02239.

Ebihara, Y., M.-C. Fok, R. A. Wolf, T. J. Immel, and T. E. Moore (2004), Influence of ionosphere conductivity on the ring current, *J. Geophys. Res.*, *109*, A08205, doi:10.1029/2003JA010351.

Ebihara, Y., N. Nishitani, T. Kikuchi, T. Ogawa, K. Hosokawa, M.-C. Fok, and M. F. Thomsen (2009), Dynamical property of storm time subauroral rapid flows as a manifestation of complex structures of the plasma pressure in the inner magnetosphere, *J. Geophys. Res.*, *114*, A01306, doi:10.1029/2008JA013614.

Fok, M.-C., R. A. Wolf, R. W. Spiro, and T. E. Moore (2001), Comprehensive computational model of Earth's ring current, *J. Geophys. Res.*, *106*, 8417–8424, doi:10.1029/2000JA000235.

Foster, J. C., and W. J. Burke (2002), SAPS: A new categorization for sub-auroral electric fields, *Eos Trans. AGU*, *83*(36), 393–394, doi:10.1029/2002EO000289.

Galand, M., and A. D. Richmond (2001), Ionospheric electrical conductances produced by auroral proton precipitation, *J. Geophys. Res.*, *106*(A1), 117–125, doi:10.1029/1999JA002001.

Gkioulidou, M., C.-P. Wang, L. R. Lyons, and R. A. Wolf (2009), Formation of the Harang reversal and its dependence on plasma sheet conditions: Rice convection model simulations, *J. Geophys. Res.*, *114*, A07204, doi:10.1029/2008JA013955.

Glauert, S. A., and R. B. Horne (2005), Calculation of pitch angle and energy diffusion coefficients with the PADIE code, *J. Geophys. Res.*, *110*, A04206, doi:10.1029/2004JA010851.

Glauert, S. A., R. B. Horne, and N. P. Meredith (2014), Three-dimensional electron radiation belt simulations using the BAS Radiation Belt Model with new diffusion models for chorus, plasmaspheric hiss, and lightning-generated whistlers, *J. Geophys. Res. Space Physics*, *119*, 268–289, doi:10.1002/2013JA019281.

Harang, L. (1946), The mean field of disturbance of polar geomagnetic storms, *Terr. Magn. Atmos. Electric.*, *51*(3), 353–380.

Hardy, D. A., M. S. Gussenhoven, R. Raistrick, and W. J. Mcneil (1987), Statistical and functional representations of the pattern of auroral energy flux, number flux, and conductivity, *J. Geophys. Res.*, *92*(A11), 12,275–12,294.

Horne, R. B., R. M. Thorne, N. P. Meredith, and R. R. Anderson (2003), Diffuse auroral electron scattering by electron cyclotron harmonic and whistler mode waves during an isolated substorm, *J. Geophys. Res.*, *108*(A7), 1290, doi:10.1029/2002JA009736.

Horne, R. B., T. Kersten, S. A. Glauert, N. P. Meredith, D. Boscher, A. Sicard-Piet, R. M. Thorne, and W. Li (2013), A new diffusion matrix for whistler mode chorus waves, *J. Geophys. Res. Space Physics*, *118*, 6302–6318, doi:10.1002/jgra.50594.

Horwitz, J. L. (1987), Core plasma in the magnetosphere, *Rev. Geophys.*, *25*(3), 579–587, doi:10.1029/RG025i003p00579.

Huba, J. D., and S. Sazykin (2014), Storm time ionosphere and plasmasphere structuring: SAMI3-RCM simulation of the 31 March 2001 geomagnetic storm, *Geophys. Res. Lett.*, *41*, 8208–8214, doi:10.1002/2014GL062110.

Huba, J. D., S. Sazykin, and A. Coster (2017), SAMI3-RCM simulation of the 17 March 2015 geomagnetic storm, *J. Geophys. Res. Space Physics*, *122*, 1246–1257, doi:10.1002/2016JA023341.

Ilie, R., M. W. Liemohn, G. Toth, and R. M. Skoug (2012), Kinetic model of the inner magnetosphere with arbitrary magnetic field, *J. Geophys. Res.*, *117*, A04208, doi:10.1029/2011JA017189.

Jordanova, V. K., Y. S. Miyoshi, S. Zaharia, M. F. Thomsen, G. D. Reeves, D. S. Evans, C. G. Mouikis, and J. F. Fennell (2006), Kinetic simulations of ring current evolution during the Geospace Environment Modeling challenge events, *J. Geophys. Res.*, *111*, A11S10, doi:10.1029/2006JA011644.

Jordanova, V. K., S. Zaharia, and D. T. Welling (2010), Comparative study of ring current development using empirical, dipolar, and self-consistent magnetic field simulations, *J. Geophys. Res.*, *115*, A00J11, doi:10.1029/2010JA015671.

Jordanova, V. K., D. T. Welling, S. G. Zaharia, L. Chen, and R. M. Thorne (2012), Modeling ring current ion and electron dynamics and plasma instabilities during a high-speed stream driven storm, *J. Geophys. Res.*, *117*, A00L08, doi:10.1029/2011JA017433.

Kelley, M. C., and R. A. Heelis (1989), *The Earth's Ionosphere [Electronic Resource]: Plasma Physics and Electrodynamics*, Academic Press, Boston, Mass.

Khazanov, G. V., M. W. Liemohn, T. S. Newman, M.-C. Fok, and R. W. Spiro (2003), Self-consistent magnetosphere-ionosphere coupling: Theoretical studies, *J. Geophys. Res.*, *108*, 1122, doi:10.1029/2002JA009624.

Li, L. Y., J. Yu, J. B. Cao, D. Zhang, X. H. Wei, Z. J. Rong, J. Y. Yang, and H. S. Fu (2013), Rapid loss of the plasma sheet energetic electrons associated with the growth of whistler mode waves inside the bursty bulk flows, *J. Geophys. Res. Space Physics*, *118*, 7200–7210, doi:10.1002/2013JA019109.

Liemohn, M. W., A. J. Ridley, D. L. Gallagher, D. M. Ober, and J. U. Kozyra (2004), Dependence of plasmaspheric morphology on the electric field description during the recovery phase of the 17 April 2002 magnetic storm, *J. Geophys. Res.*, *109*, A03209, doi:10.1029/2003JA010304.

Liemohn, M. W., A. J. Ridley, P. C. Brandt, D. L. Gallagher, J. U. Kozyra, D. M. Ober, D. G. Mitchell, E. C. Roelof, and R. DeMajistre (2005), Parametric analysis of nightside conductance effects on inner magnetospheric dynamics for the 17 April 2002 storm, *J. Geophys. Res.*, *110*, A12S22, doi:10.1029/2005JA011109.

Liu, X., W. Liu, J. B. Cao, H. S. Fu, J. Yu, and X. Li (2015), Dynamic plasmapause model based on THEMIS measurements, *J. Geophys. Res. Space Physics*, *120*, 10,543–10,556, doi:10.1002/2015JA021801.

Matsui, H., V. K. Jordanova, J. M. Quinn, R. B. Torbert, and G. Paschmann (2004), Derivation of electric potential patterns in the inner magnetosphere from Cluster EDI data: Initial results, *J. Geophys. Res.*, *109*, A10202, doi:10.1029/2003JA010319.

Matsui, H., R. B. Torbert, H. E. Spence, Y. V. Khotyaintsev, and P. A. Lindqvist (2013), Revision of empirical electric field modeling in the inner magnetosphere using Cluster data, *J. Geophys. Res. Space Physics*, *118*, 4119–4134, doi:10.1002/jgra.50373.

Moen, J., and A. Brekke (1993), The solar flux influence on quiet time conductances in the auroral ionosphere, *Geophys. Res. Lett.*, *20*, 971–974, doi:10.1029/92GL02109.

Newell, P. T., T. Sotirelis, and S. Wing (2009), Diffuse, monoenergetic, and broadband aurora: The global precipitation budget, *J. Geophys. Res.*, *114*, A09207, doi:10.1029/2009JA014326.

Ni, B., R. M. Thorne, Y. Y. Shprits, and J. Bortnik (2008), Resonant scattering of plasma sheet electrons by whistler-mode chorus: Contribution to diffuse auroral precipitation, *Geophys. Res. Lett.*, *35*, L11106, doi:10.1029/2008GL034032.

Nishimura, Y., A. Shinbori, T. Ono, M. Iizima, and A. Kumamoto (2006), Storm-time electric field distribution in the inner magnetosphere, *Geophys. Res. Lett.*, *33*, L22102, doi:10.1029/2006GL027510.

Nishimura, Y., A. Shinbori, T. Ono, M. Iizima, and A. Kumamoto (2007), Evolution of ring current and radiation belt particles under the influence of storm-time electric fields, *J. Geophys. Res.*, *112*, A06241, doi:10.1029/2006JA012177.

Richmond, A. D., and Y. Kamide (1988), Mapping electrodynamic features of the high-latitude ionosphere from localized observations: Technique, *J. Geophys. Res.*, *93*(A6), 5741–5759, doi:10.1029/JA093iA06p05741.

Ridley, A., T. Gombosi, and D. Dezeeuw (2004), Ionospheric control of the magnetosphere: Conductance, *Ann. Geophys.*, *22*, 567–584, doi:10.5194/angeo-22-567-2004.

Ridley, A. J., and M. W. Liemohn (2002), A model-derived storm time asymmetric ring current driven electric field description, *J. Geophys. Res.*, *107*(A8), 1151, doi:10.1029/2001JA000051.

Robinson, R. M., R. R. Vondrak, K. Miller, T. Dabbs, and D. Hardy (1987), On calculating ionospheric conductances from the flux and energy of precipitating electrons, *J. Geophys. Res.*, *92*, 2565–2569, doi:10.1029/JA092iA03p02565.

Rowland, D. E., and J. R. Wygant (1998), Dependence of the large-scale, inner magnetospheric electric field on geomagnetic activity, *J. Geophys. Res.*, *103*(A7), 14,959–14,964, doi:10.1029/97JA03524.

Sckopke, N. (1966), A general relation between the energy of trapped particles and the disturbance field near the Earth, *J. Geophys. Res.*, *71*, 3125–3130, doi:10.1029/JZ071i013p03125.

Stern, D. P. (1975), The motion of a proton in the equatorial magnetosphere, *J. Geophys. Res.*, *80*, 595–599, doi:10.1029/JA080i004p00595.

Toffoletto, F., S. Sazykin, R. Spiro, and R. Wolf (2003), Inner magnetospheric modeling with the Rice Convection Model, *Space Sci. Rev.*, *107*, 175–196, doi:10.1023/A:1025532008047.

Tsyganenko, N. A. (1989), A magnetospheric magnetic field model with a warped tail current sheet, *Planet. Space Sci.*, *37*, 5–20, doi:10.1016/0032-0633(89)90066-4.

Vasyliunas, V. M. (1970), Mathematical models of magnetospheric convection and its coupling to the ionosphere, in *Particles and Field in the Magnetosphere, Astrophysics and Space Science Library*, vol. 17, edited by B. M. McCormack and and A. Renzini, pp. 60–71, Springer, Netherlands.

Volland, H. (1973), A semiempirical model of large-scale magnetospheric electric fields, *J. Geophys. Res.*, *78*, 171–180, doi:10.1029/JA078i001p00171.

Wang, H., H. Lühr, A. Ridley, and T. Huang (2014), The spatial distribution of region 2 field-aligned currents relative to subauroral polarization stream, *Ann. Geophys.*, *32*(5), 533–542, doi:10.5194/angeo-32-533-2014.

Weimer, D. R. (2001), An improved model of ionospheric electric potentials including substorm perturbations and application to the Geospace Environment Modeling November 24, 1996, event, *J. Geophys. Res.*, *106*, 407–416, doi:10.1029/2000JA000604.

Weimer, D. R. (2005), Improved ionospheric electrodynamic models and application to calculating joule heating rates, *J. Geophys. Res.*, *110*, A05306, doi:10.1029/2004JA010884.

Young, D. T., H. Balsiger, and J. Geiss (1982), Correlations of magnetospheric ion composition with geomagnetic and solar activity, *J. Geophys. Res.*, *87*(A11), 9077–9096, doi:10.1029/JA087iA11p09077.

Yu, Y., V. Jordanova, S. Zou, R. Heelis, M. Ruohoniemi, and J. Wygant (2015), Modeling subauroral polarization streams during the 17 March 2013 storm, *J. Geophys. Res. Space Physics*, *120*, 1738–1750, doi:10.1002/2014JA020371.

Yu, Y., V. K. Jordanova, A. J. Ridley, J. M. Albert, R. B. Horne, and C. A. Jeffery (2016), A new ionospheric electron precipitation module coupled with RAM-SCB within the geospace general circulation model, *J. Geophys. Res. Space Physics*, *121*, 8554–8575, doi:10.1002/2016JA022585.

Zaharia, S., C. Cheng, and K. Maezawa (2004), 3-D force-balanced magnetospheric configurations, *Ann. Geophys.*, *22*, 251–265, doi:10.5194/angeo-22-251-2004.

Zaharia, S., V. K. Jordanova, M. F. Thomsen, and G. D. Reeves (2006), Self-consistent modeling of magnetic fields and plasmas in the inner magnetosphere: Application to a geomagnetic storm, *J. Geophys. Res.*, *111*, A11S14, doi:10.1029/2006JA011619.

Zaharia, S., V. K. Jordanova, D. Welling, and G. Tóth (2010), Self-consistent inner magnetosphere simulation driven by a global MHD model, *J. Geophys. Res.*, *115*, A12228, doi:10.1029/2010JA015915.

Zhang, D., J. B. Cao, X. H. Wei, and L. Y. Li (2015), New technique to calculate electron Alfvén layer and its application in interpreting geosynchronous access of PS energetic electrons, *J. Geophys. Res. Space Physics*, *120*, 1675–1683, doi:10.1002/2014JA020670.

Zou, S., L. R. Lyons, C.-P. Wang, A. Boudouridis, J. M. Ruohoniemi, P. C. Anderson, P. L. Dyson, and J. C. Devlin (2009), On the coupling between the harang reversal evolution and substorm dynamics: A synthesis of SuperDARN, DMSP, and IMAGE observations, *J. Geophys. Res.*, *114*, A01205, doi:10.1029/2008JA013449.